HHS Public Access

Author manuscript

Nat Phys. Author manuscript; available in PMC 2020 September 03.

Published in final edited form as:

Nat Phys. 2020 January ; 16(1): 101–108. doi:10.1038/s41567-019-0680-8.

Cell swelling, softening and invasion in a three-dimensional breast cancer model

Yu Long Han[1], **Adrian F. Pegoraro**[2,3], **Hui Li**[4,5], **Kaifu Li**[6], **Yuan Yuan**[3], **Guoqiang Xu**[1], **Zichen Gu**[1], **Jiawei Sun**[1], **Yukun Hao**[1], **Satish Kumar Gupta**[1], **Yiwei Li**[1], **Wenhui Tang**[1], **Xiao Tang**[6], **Lianghong Teng**[6], **Jeffrey J. Fredberg**[7], **Ming Guo**[1,*]

[1]Department of Mechanical Engineering, Massachusetts Institute of Technology, Cambridge, MA, 02139, USA

[2]Department of Physics, University of Ottawa, Ottawa, ON, K1N 6N5, Canada

[3]Harvard John A. Paulson School of Engineering and Applied Sciences, Cambridge, MA, 02138, USA

[4]School of Systems Science, Beijing Normal University, Beijing 100875, P.R. China

[5]Key Laboratory of Soft Matter Physics, Institute of Physics, Chinese Academy of Sciences, Beijing 100190, P.R. China

[6]Xuanwu Hospital, Capital Medical University, Beijing, 100053, P.R. China

[7]Harvard T. H. Chan School of Public Health, Boston, MA, 02115, USA

Abstract

Sculpting of structure and function of three-dimensional multicellular tissues depend critically on the spatial and temporal coordination of cellular physical properties, yet the organizational principles that govern these events, and their disruption in disease, remain poorly understood. Using a multicellular mammary cancer organoid model, here we map in three dimensions the spatial and temporal evolution of positions, motions, and physical characteristics of individual cells. Compared with cells in the organoid core, cells at the organoid periphery and the invasive front are found to be systematically softer, larger and more dynamic. These mechanical changes are shown to arise from supracellular fluid flow through gap junctions, suppression of which delays transition to an invasive phenotype. Together, these findings highlight the role of

[*]**Correspondence**: Ming Guo, *Massachusetts Institute of Technology, Cambridge, MA 02139, USA., Phone: +1 (617) 324-0136,* guom@mit.edu.

Contributions

Y.L.H. and M.G. designed the experiments; M.G. supervised the project; Y.L.H., H.L., Z.G., K.L., X.T., Y.Y., Y.L., W.T., and L.T. performed the experiments; Y.L.H., A.F.P., G.X., Z.G., J.S., Y.H. and S.K.G. developed MATLAB scripts for imaging processing and data analysis; Y.L.H., A.F.P., J.J.F. and M.G. wrote the manuscript. All authors edited and approved the manuscript.

Conflict of Interest statement:

The authors declare no conflict of interests.

Data availability. Data supporting the findings of this study are available within the article and its Supplementary Information files and from the corresponding author upon reasonable request.

Code availability. MATLAB scripts used in this work are available from the corresponding author upon reasonable request.

spatiotemporal coordination of cellular physical properties in tissue organization and disease progression.

Living cells are dynamic systems undergoing processes ranging from gene expression, intracellular dynamics and forces at the molecular level[1–3] to cell contraction, deformation and migration at the cellular level[4–10]. Within a multicellular tissue the precise control of these physical characteristics in space and time is critical for maintenance of mechanical integrity and biological function. Deviation from mechanical hemostasis is associated with diseases including aberrant wound repair, developmental abnormalities, and cancer[11–17]. In the isolated cell *in vitro*, for example, increased deformability[18–21], intracellular dynamics[22], contractility[23] and mobility have each been identified as a physical hallmark of different types of cancer[24] and have been proposed as potential targets for cancer treatment[25]. Despite the promise of *in vitro* approaches, extensive studies have shown that the mechanical properties of cells are regulated by their microenvironment including but not limited to stiffness of the surrounding matrix, cell densities and dimensions[26,27]. Hence in the context of a multicellular system in the 3D microenvironment, how physical characteristics of individual cells regulate and coordinate tumor development and invasion remains unknown.

By integrating confocal microscopy with optical tweezers, we have developed a platform to measure morphological characteristics, physical properties and migratory dynamics of individual cells throughout a growing multicellular 3D breast cancer model[11,12]. Tracking the spatiotemporal evolution of individual cells during the growing process, we find heterogeneous patterns of cellular physical characteristics which facilitate tumor cell invasion. Compared with cells in the organoid core, those at the invasive leading edge are faster, softer, and larger. Not only are the volumes of both the cell body and the nucleus larger at the invasive leading edge, but also the temporal fluctuations characterizing cytoplasmic dynamics become stronger. Blocking gap junctions significantly suppresses these changes, suggesting that supracellular fluid flow potentially drives the evolution of the observed patterns of cellular properties. Furthermore, elimination of the softer subpopulation in the cancer organoid strongly delays the transition to an invasive phenotype. Together, these findings highlight a causal role of spatiotemporal coordination of cellular physical properties, especially cell swelling and softening, in tumor development and invasive dynamics.

Epithelial cancer organoids have been widely used to model glandular epithelial cancers in 3D culture systems[28]; these models recapitulate distinguishing physiological features of epithelial tissues while also capturing the pathological features of epithelial tumors. For example, the well-ordered epithelial architecture becomes disrupted, the lumen fills with cells, and invasive branches then form[28]. To reveal the mechanical underpinnings of this process, we transfected MCF-10A human breast epithelial cells with a green fluorescent protein (GFP) tagged with nuclear-localization-signal (NLS). We then seeded these cells into a 3D interpenetrating network hydrogel composed of 5 mg/mL alginate and 4 mg/mL Matrigel[12], with a shear modulus close to 300 Pa to mimic the mechanical microenvironment of a breast carcinoma *in vivo*[12,29].

Starting from a single cell, a multicellular cluster grows and invasive branches develop over approximately 10 days (Fig. 1a–c); in accordance with recent definitions, we call this cluster a cancer organoid[30]. During the early stage, an individual MCF-10A cell proliferates to form a spherical cluster (early stage; Fig. 1a, day 3). This cell cluster grows into a larger spheroid with cells both in the core and on the periphery (middle stage; Fig. 1b, day 5). As this spheroid develops further, invasive branches extend from the main body and invade the surrounding extracellular matrix (ECM) (later stage; Fig. 1c, day 10). The phenotype observed in this 3D breast cancer model shows uncontrolled cellular proliferation, lack of cellular polarization and the initiation of matrix invasion, much like those observed *in vivo* in invasive ductal carcinomas (Fig. 1d). This contrasts with a normal acinar structure that develops when cells are seeded in soft matrix (Fig. S1).

Molecular pathways that regulate the invasion process in this model system have been well studied[11,12] but associated changes in the physical properties of cells remain largely unknown. To characterize cell mechanics in this growing epithelial cancer organoid, we used optical tweezers to perform active microrheology and thus measure the mechanical properties of the cytoplasm within individual cells. To do so, we mixed into the ECM small particles (0.5-μm diameter) that became endocytosed by individual constituent cells. These particles were dragged unidirectionally by optical tweezers at 0.5 μm/s to obtain a force-displacement relationship of the cytoplasm (illustrated in Fig. 1e), which thus characterized the cytoplasmic stiffness within each particular cell[31]. This force-displacement relationship was found to vary spatially within the growing cancer organoid (Fig. 1f, inset). To compare different regions, we spatially segmented the cancer organoid into three different populations: core, periphery and branch. At early stages only one population was evident. At middle stages, however, cells were classified as being in the core if they were within the inner 40% of the cancer organoid radius. After branches formed, a central spheroidal mass was defined and separated into core and periphery cells, with all other cells being assigned as being part of the branches (Fig. S2a). Interestingly, we found that the force required to deform the cytoplasm of cells in the core of the cancer organoid was appreciably greater than that required for cells in the periphery or in a branch (Fig. 1f, inset). To further quantify this difference, we measured an apparent modulus, E_A, of the cytoplasm by taking the average slope of the linear regime of the normalized force-displacement curve. We found that cells in the core of the cancer organoid were stiffest while cells in branches were the softest (Fig. 1f). Moreover, the range of stiffness and the population heterogeneity increased as the cancer organoid developed (Fig. 1g), consistent with findings from *in vivo* samples, where increasing mechanical heterogeneity during disease progression has been observed[32]. This evolution from a homogeneous to heterogeneous population with distinct mechanical properties is reminiscent of the epigenetic heterogeneity that has been observed in breast tumor progression[33].

Given the spatial variation observed in cell stiffness, we wondered whether cytoplasmic dynamics vary in different regions of the cancer organoid as well. To quantify cytoplasmic dynamics, we used confocal microscopy to image spontaneous fluctuations of endocytosed fluorescent particles (0.5-μm diameter) which are larger than the typical cytoskeletal mesh size (~50 nm); particle motions report the active non-equilibrium force fluctuations that arise spontaneously within the cytoplasm and thus also influence the dynamics of proteins and

organelles in the cytoplasm[22]. By tracking trajectories of these particles we calculated the mean-square displacement (MSD), $<\Delta r^2(\tau)>$, where $\Delta r(\tau)=r(t+\tau)-r(t)$. When comparing MSD for different regions of the cancer organoid, dynamics in the core were smallest, followed by periphery cells, with branch cells showing the greatest cytoplasmic dynamics (Fig. 2a). Interestingly, beyond cytoplasmic dynamics, we found similar differences in intra-nuclear dynamics; the diffusion of GFP in the cell nucleus, probed by fluorescent recovery after photobleaching, was also substantially slower in the core region as compared to the periphery of the cancer organoid (Fig. S2b–c).

While the change in intracellular dynamics was consistent with the changes in cytoplasmic stiffness, dynamics are influenced not only by the passive mechanical properties of the cytoplasm but also by active ATP-dependent force fluctuations within the cell[22]. To measure the latter we used force spectrum microscopy (FSM), which combines measurements of the spontaneous fluctuations of probe particles with the micromechanical measurement in the cytoplasm to quantify the spectrum of the aggregate force fluctuations, $<\tilde{f}^2(\omega)>$, in the cell; this force fluctuation spectrum is reflective of the total enzymatic activity[22]. Using FSM, we found that cells in the branch have the highest cytoplasmic force fluctuations, with approximately 5 times greater magnitude at 1 Hz as compared to cells in the spheroid core (Fig. 2b).

We also assessed cell motility by imaging the cancer organoid at a high spatial and temporal resolution. Full 3D images of the organoid were recorded by confocal microscopy every 10 minutes over a 24-hr period subsequent to a branch forming (Supplementary Movie 1 and 2). By tracking the position of every cell nucleus, cell tracks were constructed (Fig. 2c). From the cell tracks, migration speed of every cell in this 3D organoid was calculated. All cells were constantly migrating, but cells in the branches or in the periphery migrated faster than did cells in the core (Fig. 2d). This spatial dependence in migration speed mirrored the spatial dependence of cytoplasmic dynamics.

Cell volume is another important physiological property that is known to correlate with cell stiffness and dynamics[26,34]. To compare cell and nuclear volumes, we fluorescently labeled the whole cell by cytoplasmic staining in addition to the already GFP-NLS labeled cell nuclei, and then measured volumes using 3D confocal microscopy. In agreement with previous findings[26,35], we found over a wide range of organoid sizes that the ratio of nuclear to cell volume in individual cells remained constant (13±1%, Fig. S3), allowing us to measure nuclear volume in lieu of cell volume. At early stages of cancer organoid development, when no clear subregions exist, cells had similar nuclear volumes (Fig. 3a, day 3). As the organoid developed, nuclear volumes increased their spatially variability (Fig. 3a, day 5 and day 10); the nuclear volume of the cells strongly correlated with the relative cell position within the cancer organoid (Fig. 3b, day 5 and 10) with smaller cells in the core. The transition from the early to middle period of development led to cells in the core becoming systematically smaller (Fig. 3c, day 5). As growth continued, the cancer organoid eventually underwent an invasive transition marked by the formation and growth of branches into the ECM; while the core and periphery still displayed clearly distinct nuclear volumes, the formation of invasive branches resulted in cells with even larger nuclear volumes (Fig. 3c, day 10). Interestingly, nuclear volume of cells in the same regime also evolved as the

cancer organoid grew; cell nuclei in the core became smaller as the size of the cancer organoid increased from day 5 to 10 (Fig. 3c, blue boxes). This spatial pattern of nuclear volume was also observed in other 3D mammary cancer models using different cell lines and ECMs, such as MCF10A and MCF10AT in collagen/Matrigel system[11] (Fig. S4).

Gap junctions (GJs) are specialized intercellular connections between epithelial cells and have been widely observed in normal and malignant breast tissues[36]. They connect the cytoplasm of two neighboring cells, and thus allow molecules and ions to directly pass through[37,38]. Accumulating evidence has shown that there is a significant compressive stress within tumor tissue and 3D cancer models[39–42]. Therefore, we hypothesize that the observed volume gradient in our system is a result of supracellular fluid flow through cell-cell GJs, driven by the higher intratumor compressive stress. To test if the volume gradient is GJ dependent, we added GJ inhibitor (carbenoxolone[43], 500 μM) in our system on day 3, where the volume gradient was not yet present (Fig. 3 a and b, day 3). As the cancer organoid continued to grow, we did not observe a significant difference between nuclear volume of cells in the core and in the periphery (Fig. 3d). Similar results were observed when we used a different type of gap junction inhibitor, connexin mimetic peptides (CMPs)[44] (Fig. S5). These results suggest that the GJs within the organoid play a role in the development of the observed cellular volume pattern. Consistently, it has also been shown that externally applied mechanical stress can drive fluid flow between cells through GJs in a 2D monolayer[45] as well as 3D MCF10A clusters[46], and induce cell volume variations.

To investigate this hypothesis further, we tested if the intratumor mechanical stress[39–42] is a factor in the observed cell volume gradient. Using organoids cultured in collagen/Matrigel network, on day 5 we reduced the mechanical stresses present by releasing the organoids from the matrix confinement using collagenase. Six hours after stress release, we observed a significant increase of the cellular volume in the core and a decrease in the periphery (Fig. 3e, stress release). The initial cell volume gradient then became much weaker, suggestive of an inverse supracellular fluid flow from periphery to the core upon stress release. To further test our hypothesis that GJs play a role in supracellular fluid flow, we blocked the GJs 6 hours prior to releasing the stress, and we did not observe any significant changes in cellular volume and its gradient upon stress release (Fig. 3e, GJ inhibitor+stress release). Taken together, these results indicate that the imbalance of intratumor stress drives a fluid flow through GJs in the 3D cancer model system, which results in the swell and shrink of cells in the periphery and in the core respectively.

For both isolated cells and confluent monolayers in 2D, cell volume has been found to vary with cell stiffness and internal dynamics, with a decrease in cell volume corresponding to an increase in cell stiffness and a decrease in internal dynamics[26,34]. Similar trends prevailed in the developing 3D cancer organoid. Cells in the core became smaller, stiffer and less dynamic. By contrast, cells in the branches became bigger, softer and more dynamic. Interestingly, when we tracked individual cell positions over time, we found that cells transit from the core to the periphery or conversely (Figs. S6a and S6b). Moreover, if we track a cell in a branch it tends to be swollen, but as it moves toward the core it shrinks, and conversely for tracking a cell in the core (Fig. S6c and S6d); as a cell transits in the cancer organoid it adjusts its physical properties to its local microenvironment.

The responsiveness of cell volume to its local microenvironment raises the question as to whether similar variability of cell volume exists in real tumor samples. To answer this question, we obtained grade-2 ER+ invasive-ductal-carcinoma human breast cancer tissue samples from a patient, and then fixed and sectioned each sample prior to staining and imaging with confocal microscopy (Fig. 4a and 4b). Within the tumor mass, spheroidal, acinar clusters of cells surrounded by basement membrane were evident (Fig. 4c and Supplementary Movie 3), which share similar characteristics with our 3D cancer model. In such spheroidal acinar clusters, we found that nuclear volume increased as the distance from the center increased (Fig. 4d), consistent with our model system. Cells in the core had smaller volume while invasive cells that appear to have escaped from the main cluster had larger volume (Fig. 4e).

These findings raise the interesting question as to whether swelling and softening of peripheral cells are important factors in invasive dynamics. To investigate this further, we artificially manipulated cell stiffness and volume of peripheral cells. For example, we changed the osmotic pressure to either compress (with additional 2% PEG300) or swell (with additional 10% water) the cells on day 3, before the formation of various subpopulations (Fig. 5a–c). We also tried increasing cell stiffness using the chemotherapy medication daunorubicin (0.5 μM), Jasplakinolide (5 μM)[47] or overexpression of an actin crosslinking protein α-Actinin. We found that the volume of cells in the periphery changed, while little change was observed in the core (Fig. 5f). The decrease or increase in cell volume was accompanied by a corresponding increase or decrease in cell stiffness (Fig. 5f). Interestingly, long-term exposure to any of these interventions did not significantly impair cell proliferation; the projected area of individual growing cancer organoids increased over time in a similar fashion compared to those in the control medium (Fig. 5d). Surprisingly, however, the invasion changed dramatically compared to the control case, where invasiveness was quantified as the percentage of cancer organoids that formed invasive branches after 11 days in each sample, with softer peripheral cells leading to greater invasiveness (Fig. 5e, Fig. S7). Furthermore, we used GJ inhibitors (carbenoxolone[43], 500 μM or CMPs [44], 600 μM) to perturb the spontaneous cell swelling and softening process in our system on day 3 (Fig. 5f), and found that the invasion of the tumor cells was also delayed (Fig. 5e). To exclude the possibility that GJ inhibitors directly impact cell mechanics, we measured the cytoplasmic stiffness of isolated MCF10A cells with GJ inhibitors on 2D surface and found that both GJ inhibitors did not affect cytoplasmic stiffness (Fig. S8). Taken together, by controlling the volume and stiffness of the peripheral cells, the invasive behavior of our 3D cancer model was significantly altered.

Understanding how mechanical changes of cells enables disease advancement is critical in determining how cancer progresses. The invasion of MCF10A clusters has previously been shown to depend on ECM mechanics through PI3K activation[11,12,48]; we indeed confirm that this is critical for disease initiation (Fig. S9–S10). However, after this initial stage of disease progression we found that mechanical heterogeneity increased giving rise to larger, softer cells and enhanced invasiveness. For isolated cells in 3D culture, cell-matrix interactions can potentially lead to cell volume increase[49] and this cannot be excluded from playing a role for peripheral cells. Nonetheless, the inhibition of GJs interfered with cell volume change during growth and stress release, indicating that fluid flow across cell

boundaries plays a role in mechanical pattern formation. The role of GJs in cancer progression is still under debate, with both promotion and suppression of invasiveness having been observed across various types of cancers and GJs[50]. Our results hint at a purely physical mechanism by which GJs can affect cancer progression. Changing water content of cells, and hence the degree of molecular crowding[26,34], will affect a wide-range of downstream cell functions and properties. As such, our emerging physical picture of tumor progression is now seen to include 3D spatiotemporal evolution of cellular physical properties.

Methods

Cancer organoid culture and immunofluorescence staining.

The mammary epithelial cancer organoid with invasive phenotype was cultured and induced following a previously established protocol[11,12]. Briefly, MCF-10A cells (ATCC) were cultured in DMEM/F12 medium (Invitrogen, No. 11965–118) supplemented with 5% horse serum (Invitrogen, No. 16050–122), 20 ng/mL EGF (Peprotech, AF-100–15), 0.5 μg/mL hydrocortisone (Sigma No. H-0888), 100 ng/mL cholera toxin (Sigma, No. C-8052), 10 μg/mL insulin (Sigma, No. I-1882) and 1% penicillin and streptomycin (ThermoFisher, No. 15140122). The cells were collected using 0.05 % trypsin-EDTA solution (ThermoFisher, No. 25300054) after they reached confluence within T-25 flasks in a normal cell culture incubator, and mixed with the gel precursor solution at a low cell concentration (10^4/mL) to avoid interaction between cancer organoids. For alginate/Matrigel interpenetrating network hydrogels, the gel was composed of alginate (FMC Biopolymer) and Matrigel (Corning, No. 354234) with final concentrations of 5 mg/mL and 4 mg/mL, respectively. The gel precursor with cells was put in the cell culture incubator for gelation. One hour later, additional complete culture medium was added to keep the gel hydrated. Cancer organoids developed in the 3D gels in the following ~10 days. For collagen/Matrigel system, the gel was composed of 3.5 mg/mL collagen and 0.5 mg/mL Matrigel. MCF10AT cell line is a gift from Jeffrey Nickerson at University of Massachusetts Medical School and was cultured as the same condition of MCF10A cell line.

For immunohistochemical staining, the cancer organoids were cultured from normal MCF10A cells (without GFP-NLS). The 3D gel with cancer organoids embedded was fixed with 4% paraformaldehyde (PFA) at room temperature for 30 min. To increase the permeability of the cell membrane, the gel was immersed in PBS supplied with 0.2% Triton X-100 (2 hr, room temperature). Then the sample was blocked with 0.5% BSA in PBS for 5 hr at room temperature, and subsequently incubated overnight at 4 °C with primary antibodies for Cytokeratin 8 (1:300 diluted in PBS, Santa Cruz Biotechnology, sc-8020), Cytokeratin 14 (1:300 diluted in PBS, Santa Cruz Biotechnology, sc-53253), Phospho-Akt (1:200 diluted in PBS, Cell Signaling, 9271T), β-catenin (1:300 diluted in PBS, Santa Cruz Biotechnology, sc-7963), Integrin β4 (1:300 diluted in PBS, Santa Cruz Biotechnology, sc-13543) or laminin-5 (1:300 diluted in PBS, Santa Cruz Biotechnology, sc-13587). Corresponding secondary antibodies were added and incubated for another night at 4 °C (1:800, ThermoFisher, A-11001 or A11008). Finally, DAPI (ThermoFisher, D1306) was

added for another 4 hr to stain cell nuclei. After each step, the samples were washed with PBS for at least 6 hr.

Optical tweezer measurement.

The laser beam (10W, 1064 nm) was tightly focused through a series of Keplerian beam expanders and a high numerical aperture objective (100 × 1.45, oil, Nikon). A high-resolution quadrant detector was used for position detection. To measure mechanical properties of the cytoplasm, 0.5-μm diameter latex particles (Sigma, L9654) were embedded in the gel and were endocytosed by the cells as they grew into cancer organoids. The linear region of the detector and the trap stiffness were calibrated with the same bead using an active power-spectrum method and equipartition theorem[31,51,52]. The endocytosed bead was dragged at a constant velocity of 0.5 μm/s by the optical trap, and the force-displacement curve of the local cytoplasm was recorded. To calculate the apparent modulus (E_A), the force and displacement were normalized by the cross-section area and the diameter of the particle respectively. The slope in the linear range of the normalized force-displacement curve was taken as the apparent modulus.

Force spectrum microscopy (FSM).

FSM combines measurements of the spontaneous fluctuation of probe particles with the micromechanical measurement in the cytoplasm to quantify the spectrum of the aggregate force fluctuations, $\langle f^2(\omega)\rangle$, in the cell which in turn is reflective of total enzymatic activity[22]. To measure the spontaneous fluctuation of the cytoplasm, 0.5-μm-diameter fluorescent particles (Sigma, L5530) were embedded in the gel and were endocytosed by the cells as they grew into cancer organoids. The motions of the particles within the cytoplasm were recorded with a 10 ms interval using confocal microscopy. Particle centers were determined in each frame, and the trajectories of particles were obtained by minimizing the overall displacement between consecutive frames as demonstrated previously[22,53], using a customized particle tracking algorithm. Time and ensemble averaged MSD, $\langle \Delta r^2(\tau)\rangle$, was then calculated. The force spectrum was calculated through $\langle f^2(\omega)\rangle = |K(\omega)|^2\langle r^2(\omega)\rangle$, where $\langle r^2(\omega)\rangle$ was obtained through the Fourier transform of MSD and the cytoplasmic spring constant $K(\omega)$ was obtained from the optical tweezer measurement with a power law assumption, $K(\omega) = K(\omega = 1\ \text{Hz})\omega^{\beta}$ with $\beta = 0.15$.[22,54]

Cell dynamics within the growing cancer organoid.

To track the movement of individual cells, cancer organoids of GFP-NLS labeled cells at different stages (day 3, 5, 10) were imaged every 10 min for 24 hr in a customized incubator (5% CO_2, 37°C, 95% humidity) on a confocal microscope (Leica, TCL SP8). The 3D positions of cell nuclei were determined at each frame and the trajectory of each individual cell was determined using the same particle tracking method and algorithm, as described above. The velocity of cells can be calculated from the adjacent positions on the trajectory of each cell.

Cell and nuclear volume measurement.

To visualize the cell nucleus, the MCF-10A cell line was transfected with GFP-NLS using lentivirus (Essen Bioscience, Cat. No. 4475). Stable cell lines were selected in puromycin containing culture medium (ThermoFisher, Cat. No. A1113802, 0.4 mg/mL). To study the volume evolution during growth of the cancer organoid, cancer organoids were formed in the hydrogel and cultured in a customized incubator (5% CO_2, 37°C, 95% humidity) on a confocal microscope (Leica, TCL SP8). The 3D conformation of the cancer organoid was recorded every 6 hr for 2 weeks. Then the 3D structure of individual cell nuclei within a cancer organoid was reconstructed and the nuclear volume was calculated by counting the voxels contained within the 3D structure using a customized algorithm in Matlab. Deconvolution (Huygens software) was applied to the image before we calculated the volume, which helps improve the z resolution of traditional confocal microscopy. To estimate the error in volume calculation from anisotropic resolution of the confocal microscopy, we repeated our volume measurements using stimulated emission depletion (STED) microscopy using a superresolution mode in z direction (~250 nm), which is similar to the resolution in x-y plane, to provide an isotropic volume reconstruction. We found a consistent volume pattern, as shown in Fig. S11a. Additionally, we imaged the same cancer spheroid with confocal microscopy and superresolution mode in STED microscopy, and compared cell volume measurement of each cell with these two methods and found consistent results (Fig. S11b).

To calculate the distance of a cell to the center of the cancer organoid, the center of each individual cell was determined by locating the local intensity maximum within the nucleus, and the center of the cancer organoid was calculated as the geometric center of the shape formed with all the cells. Cells were classified as being in the core if they were within the inner 40% of the cancer organoid radius at middle stage. After branches formed, a central spheroidal mass was defined and separated into core and periphery cells, with all other cells being assigned as being part of the branches. The cell nuclear volume distribution using this geometrical categorization is consistent with the results using molecular signatures as metric[55], as shown in Fig. S12. To obtain the nuclear volume heat map, we took a 20-μm-thickness section at the middle plane of the cancer organoid and projected each individual cell into the x-y plane, and the nuclear volume at each location (6.5 μm×6.5 μm grids on the x-y plane) was obtained by averaging nuclear volumes of all cells going through this particular location during a 2-hr window. To measure the cell volume, the GFP-NLS expressing MCF10A cells were incubated with cell tracker deep red dye (ThermoFisher, C34565), and mixed with non-fluorescent ones (without cell tracker red) to make the individual fluorescent cells distinguishable from their neighbors within the formed cancer organoid; these cancer organoids for cell volume measurement were formed using PEG-based microwell. Then the 3D morphology of both nucleus and cell body were imaged with confocal microscopy and volumes were calculated with the same algorithm in Matlab.

Human tissue.—Human tissue, including the normal breast tissue and tumor tissue, were obtained with the pre-approval of the Institutional Review Board at the Xuanwu Hospital, Beijing, China. Invasive-ductal-carcinoma samples were obtained from patients undergoing surgical removal while the pathologically normal breast tissue were obtained 2 cm away

from the tumor lesions in the same patient. Informed consent or assent was obtained from all patients and/or their parent or legal guardian as appropriate. To measure the nuclear volume within surgical tumor samples, these samples were sectioned and fixed with 4% paraformaldehyde for 1 hr. Then the central section crossing the tumor mass center was stained with Hoechst 33342 (Sigma, 14533) for another hour to visualize cell nuclei and washed 3 times with PBS. The 3D structure of the tumor slice was imaged with confocal microscopy and volume was calculated as described above. To exclude the lymphocytes for analysis, we labeled the pan-cytokeratin (a common epithelial cell maker for human, ThermoFisher, MA5–13156) in patient samples using antibodies and found that the tumor tissue indeed contains many pan-cytokeratin negative cells, suggestive of non-cancer cells (Fig. S13a). However, we rarely find lymphocytes near the invasive acinar-like structures and almost all the cells within the structure are positive of pan-cytokeratin (Fig. S13b).

Mechanical and chemical perturbations.

For osmotic compression experiments, PEG (Sigma, No. 90878, 300 MW) was added to complete culture media to a final concentration of 2% (v/v) either on day 3 (long-term) or day 5 (short-term). To record the growth of the cancer organoids in the long-term experiments, we frequently recorded bright-field images of cancer organoids for the following 10 days after osmotic compression, and the areas of the cancer organoids were quantified using ImageJ. To study the effect of osmotic compression on cell nuclear volume and cell stiffness within the cancer organoid, we took high-resolution 3D images before and after a 12-hr osmotic compression, and the cell nuclear volume and cells stiffness were analyzed as described above. Alternatively, we added common drugs including 0.5 μM daunorubicin (Sigma, D8809) or 5 μM Jasplakinolide (Santa Cruz Biotechnology, sc-202191), or overexpressed α-Actinin (Addgene, 54975) using Lipofectamine 3000 (ThermoFisher Scientific, L3000001) on day 3 to increase the stiffness of the cells within cancer organoids, and the growth of cancer organoids was recorded for 10 days. To investigate the effect of osmotic compression on organoid proliferation and apoptosis, we performed immunostaining of Ki67 (Cell Signaling, 9129S) and caspase-3 (ThermoFisher Scientific, C10423) and found that these interventions did not affect cell proliferation or induce apoptosis in our system (Fig. S14). To investigate the role of PI3K pathway in the evolution of the cellular physical properties during the growing of cancer organoid, we added 20 μM of LY294002 (Sigma, L9908) to inhibit PI3K on day 3 and the growth of the cancer organoids were recorded for 10 days thereafter. The cell nuclear volume and stiffness were measured on day 10. To block the gap junctional communication between neighbor cells within the cancer organoids, either 500 μM carbenoxolone (Sigma, C4790) or a mixture of (37,43)Gap 27 (Anaspec Inc, AS-62642, 300 μM) and (40)Gap 27 (Anaspec Inc, AS-62642, 300 μM) connexin mimetic peptides was added on day 3.

Statistics.

Two-tailed Student's *t*-test was used when comparing the difference between two groups. For comparison between multiple groups, one-way ANOVA with the Tukey method was used. In all cases, *P<0.05; **P < 0.01; ***P<0.001. In all box plots, the boxes represent the interquartile range between first and third quartiles, whereas the whiskers represent the 95% and 5% values, and the squares represent the average.

Supplementary Material

Refer to Web version on PubMed Central for supplementary material.

Acknowledgements

This work was supported by National Cancer Institute Grant 1U01CA202123. J.F. is also supported by National Institute of Health grants R01HL148152 and PO1HL120839. M.G. also acknowledges support from the Department of Mechanical Engineering at Massachusetts Institute of Technology.

References

1. Rigato A, Miyagi A, Scheuring S & Rico F High-frequency microrheology reveals cytoskeleton dynamics in living cells. Nat. Phys 13, 771–775 (2017). [PubMed: 28781604]
2. Fenz SF et al. Membrane fluctuations mediate lateral interaction between cadherin bonds. Nat. Phys 13, 906 (2017).
3. Tanimoto H, Sallé J, Dodin L & Minc N Physical forces determining the persistency and centring precision of microtubule asters. Nat. Phys 14, 848–854 (2018). [PubMed: 30079097]
4. Nam S & Chaudhuri O Mitotic cells generate protrusive extracellular forces to divide in three-dimensional microenvironments. Nat. Phys 14, 621–628 (2018).
5. Serra-Picamal X et al. Mechanical waves during tissue expansion. Nat. Phys 8, 628–634 (2012).
6. Ingber DE et al. in Mechanical Engineering of the Cytoskeleton in Developmental Biology Vol. 150 (ed Gordon Richard) 173–224 (Elsevier, 1994).
7. Tambe DT et al. Collective cell guidance by cooperative intercellular forces. Nat. Mater 10, 469 (2011). [PubMed: 21602808]
8. Xue X et al. Mechanics-guided embryonic patterning of neuroectoderm tissue from human pluripotent stem cells. Nat. Mater 17, 633–641 (2018). [PubMed: 29784997]
9. Karzbrun E, Kshirsagar A, Cohen SR, Hanna JH & Reiner O Human brain organoids on a chip reveal the physics of folding. Nat. Phys 14, 515 (2018). [PubMed: 29760764]
10. Trepat X & Sahai E Mesoscale physical principles of collective cell organization. Nat. Phys 14, 671–682 (2018).
11. Paszek MJ et al. Tensional homeostasis and the malignant phenotype. Cancer Cell 8, 241–254 (2005). [PubMed: 16169468]
12. Chaudhuri O et al. Extracellular matrix stiffness and composition jointly regulate the induction of malignant phenotypes in mammary epithelium. Nat. Mater 13, 970–978 (2014). [PubMed: 24930031]
13. Paszek MJ & Weaver VM The Tension Mounts: Mechanics Meets Morphogenesis and Malignancy. J Mammary Gland Biol Neoplasia 9, 325–342 (2004). [PubMed: 15838603]
14. Kumar S & Weaver VM Mechanics, malignancy, and metastasis: The force journey of a tumor cell. Cancer Metastasis Rev 28, 113–127 (2009). [PubMed: 19153673]
15. Pogoda K et al. Compression stiffening of brain and its effect on mechanosensing by glioma cells. New J. Phys 16, 075002 (2014).
16. Levental KR et al. Matrix Crosslinking Forces Tumor Progression by Enhancing Integrin Signaling. Cell 139, 891–906 (2009). [PubMed: 19931152]
17. Stowers RS et al. Matrix stiffness induces a tumorigenic phenotype in mammary epithelium through changes in chromatin accessibility. Nature Biomedical Engineering (2019).
18. Suresh S Biomechanics and biophysics of cancer cells. Acta Mater. 55, 3989–4014 (2007).
19. Guck J et al. Optical Deformability as an Inherent Cell Marker for Testing Malignant Transformation and Metastatic Competence. Biophys. J 88, 3689–3698 (2005). [PubMed: 15722433]
20. Fritsch A et al. Are biomechanical changes necessary for tumour progression? Nat. Phys 6, 730 (2010).

21. Xu W et al. Cell stiffness is a biomarker of the metastatic potential of ovarian cancer cells. PloS one 7, e46609 (2012). [PubMed: 23056368]
22. Guo M et al. Probing the Stochastic, Motor-Driven Properties of the Cytoplasm Using Force Spectrum Microscopy. Cell 158, 822–832 (2014). [PubMed: 25126787]
23. Koch TM, Münster S, Bonakdar N, Butler JP & Fabry B 3D traction forces in cancer cell invasion. PloS one 7, e33476 (2012). [PubMed: 22479403]
24. Swaminathan V et al. Mechanical stiffness grades metastatic potential in patient tumor cells and in cancer cell lines. Cancer Res 71, 5075–5080 (2011). [PubMed: 21642375]
25. Gandalovičová A et al. Migrastatics—anti-metastatic and anti-invasion drugs: promises and challenges. Trends in cancer 3, 391–406 (2017). [PubMed: 28670628]
26. Guo M et al. Cell volume change through water efflux impacts cell stiffness and stem cell fate. PNAS 114, E8618–E8627 (2017). [PubMed: 28973866]
27. Byfield FJ, Reen RK, Shentu T-P, Levitan I & Gooch KJ Endothelial actin and cell stiffness is modulated by substrate stiffness in 2D and 3D. J. Biomech 42, 1114–1119 (2009). [PubMed: 19356760]
28. Debnath J & Brugge JS Modelling glandular epithelial cancers in three-dimensional cultures. Nat. Rev. Cancer 5, 675–688 (2005). [PubMed: 16148884]
29. Acerbi I et al. Human breast cancer invasion and aggression correlates with ECM stiffening and immune cell infiltration. Integr. Biol 7, 1120–1134 (2015).
30. Simian M & Bissell MJ Organoids: a historical perspective of thinking in three dimensions. J. Cell Biol 216, 31–40 (2017). [PubMed: 28031422]
31. Hu J et al. Size- and speed-dependent mechanical behavior in living mammalian cytoplasm. PNAS 114, 9529–9534 (2017). [PubMed: 28827333]
32. Plodinec M et al. The nanomechanical signature of breast cancer. Nat. Nanotechnol 7, 757 (2012). [PubMed: 23085644]
33. McGranahan N & Swanton C Clonal Heterogeneity and Tumor Evolution: Past, Present, and the Future. Cell 168, 613–628 (2017). [PubMed: 28187284]
34. Zhou E et al. Universal behavior of the osmotically compressed cell and its analogy to the colloidal glass transition. PNAS 106, 10632–10637 (2009). [PubMed: 19520830]
35. Jovtchev G, Schubert V, Meister A, Barow M & Schubert I Nuclear DNA content and nuclear and cell volume are positively correlated in angiosperms. Cytogenetic and genome research 114, 77–82 (2006). [PubMed: 16717454]
36. Teleki I et al. Correlations of differentially expressed gap junction connexins Cx26, Cx30, Cx32, Cx43 and Cx46 with breast cancer progression and prognosis. PloS one 9, e112541 (2014). [PubMed: 25383624]
37. Staehelin LA Three types of gap junctions interconnecting intestinal epithelial cells visualized by freeze-etching. PNAS 69, 1318–1321 (1972). [PubMed: 4504340]
38. Wade MH, Trosko JE & Schindler M A fluorescence photobleaching assay of gap junction-mediated communication between human cells. Science 232, 525–528 (1986). [PubMed: 3961495]
39. Dolega M et al. Cell-like pressure sensors reveal increase of mechanical stress towards the core of multicellular spheroids under compression. Nat. Commun 8, 14056 (2017). [PubMed: 28128198]
40. Lee W et al. Dispersible hydrogel force sensors reveal patterns of solid mechanical stress in multicellular spheroid cultures. Nat. Commun 10, 144 (2019). [PubMed: 30635553]
41. Mohagheghian E et al. Quantifying compressive forces between living cell layers and within tissues using elastic round microgels. Nat. Commun 9, 1878 (2018). [PubMed: 29760452]
42. Nia HT et al. Solid stress and elastic energy as measures of tumour mechanopathology. Nat. Biomed. Eng 1, 0004 (2016). [PubMed: 28966873]
43. Manjarrez-Marmolejo J & Franco-Pérez J Gap junction blockers: an overview of their effects on induced seizures in animal models. Current neuropharmacology 14, 759–771 (2016). [PubMed: 27262601]
44. Evans WH & Boitano S Connexin mimetic peptides: specific inhibitors of gap-junctional intercellular communication. Biochem. Soc. Trans 29, 606 (2001). [PubMed: 11498037]

45. Zehnder SM et al. Multicellular density fluctuations in epithelial monolayers. Phys. Rev. E 92, 032729 (2015).
46. McLachlan E, Shao Q, Wang H. l., Langlois S & Laird DW Connexins act as tumor suppressors in three-dimensional mammary cell organoids by regulating differentiation and angiogenesis. Cancer Res 66, 9886–9894 (2006). [PubMed: 17047050]
47. Schulze C et al. Stiffening of human skin fibroblasts with age. Biophys. J 99, 2434–2442 (2010). [PubMed: 20959083]
48. Rubashkin MG et al. Force engages vinculin and promotes tumor progression by enhancing PI3K activation of phosphatidylinositol (3, 4, 5)-triphosphate. Cancer Res 74, 4597–4611 (2014). [PubMed: 25183785]
49. Lee H. p., Stowers R & Chaudhuri O Volume expansion and TRPV4 activation regulate stem cell fate in three-dimensional microenvironments. Nat. Commun 10, 529 (2019). [PubMed: 30705265]
50. Aasen T, Mesnil M, Naus CC, Lampe PD & Laird DW Gap junctions and cancer: communicating for 50 years. Nat. Rev. Cancer 16, 775 (2016). [PubMed: 27782134]
51. Han YL et al. Cell contraction induces long-ranged stress stiffening in the extracellular matrix. PNAS 115, 4075–4080 (2018). [PubMed: 29618614]
52. Hu J et al. High stretchability, strength, and toughness of living cells enabled by hyperelastic vimentin intermediate filaments. PNAS, 201903890 (2019).
53. Crocker JC & Grier DG Methods of Digital Video Microscopy for Colloidal Studies. J. Colloid Interface Sci 179, 298–310 (1996).
54. Gupta SK & Guo M Equilibrium and out-of-equilibrium mechanics of living mammalian cytoplasm. J. Mech. Phys. Solids 107, 284–293 (2017).
55. Mekhdjian AH et al. Integrin-mediated traction force enhances paxillin molecular associations and adhesion dynamics that increase the invasiveness of tumor cells into a three-dimensional extracellular matrix. Mol. Biol. Cell 28, 1467–1488 (2017). [PubMed: 28381423]

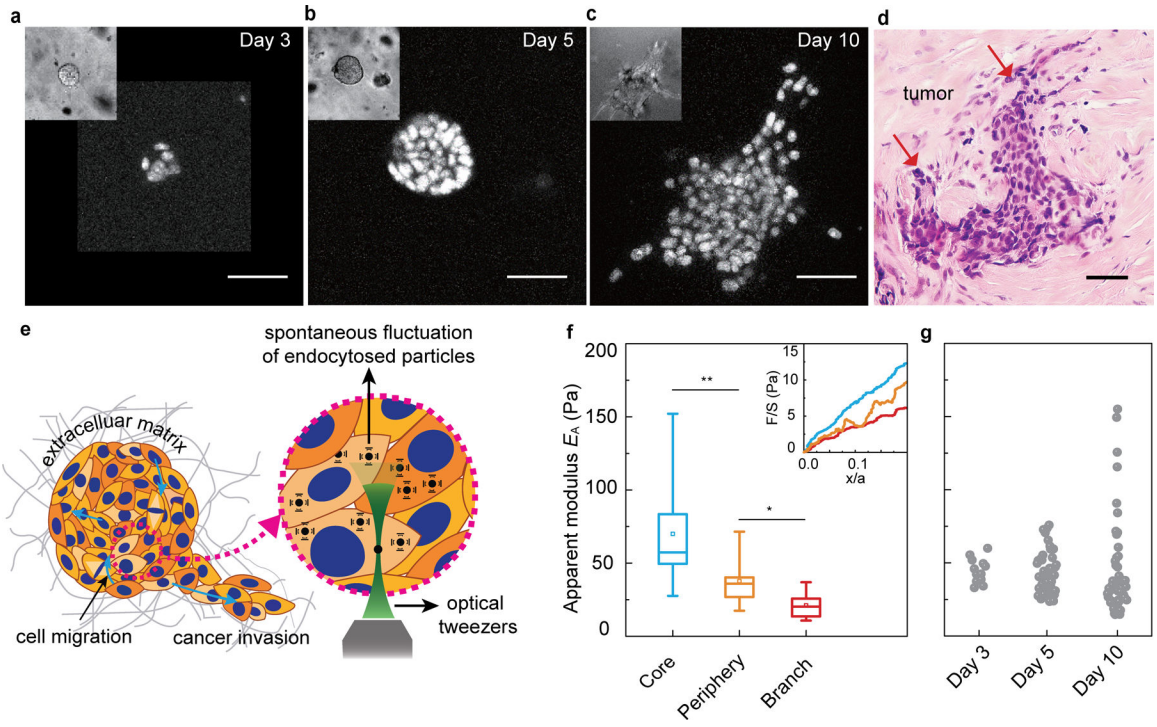

Figure 1. Evolution of heterogeneity and subpopulations of cell stiffness in the growing cancer organoid.

a-c, Cross-section images of epithelial cancer organoid developed from GFP-NLS labeled MCF-10A cells at different stages, early stage (day 3, (**a**)), middle stage (day 5, (**b**)) and later stage (day 10, (**c**)). **d**, Haemotoxylin and Eosin (H&E) stains from grade-2 ER+ invasive-ductal-carcinoma human-breast-cancer tissue samples. Tumor glands are indicated using red arrows. **e,** Schematic illustration of the cytoplasmic mechanics and dynamics measurements in a growing cancer organoid using optical tweezers. **f,** The apparent modulus, E_A, of individual cells in core (blue), periphery (orange) and branch (red) regions of the cancer organoid, quantified from slopes of the normalized force-displacement curves (inset of f). **g**, Mechanical heterogeneity of individual cells within the cancer organoid at different stages. Measurements are done in more than 3 independent cancer organoids for **f** and **g**. *P<0.05; **P < 0.01; ***P<0.001. Scale bars in **a-d** indicate 50 μm.

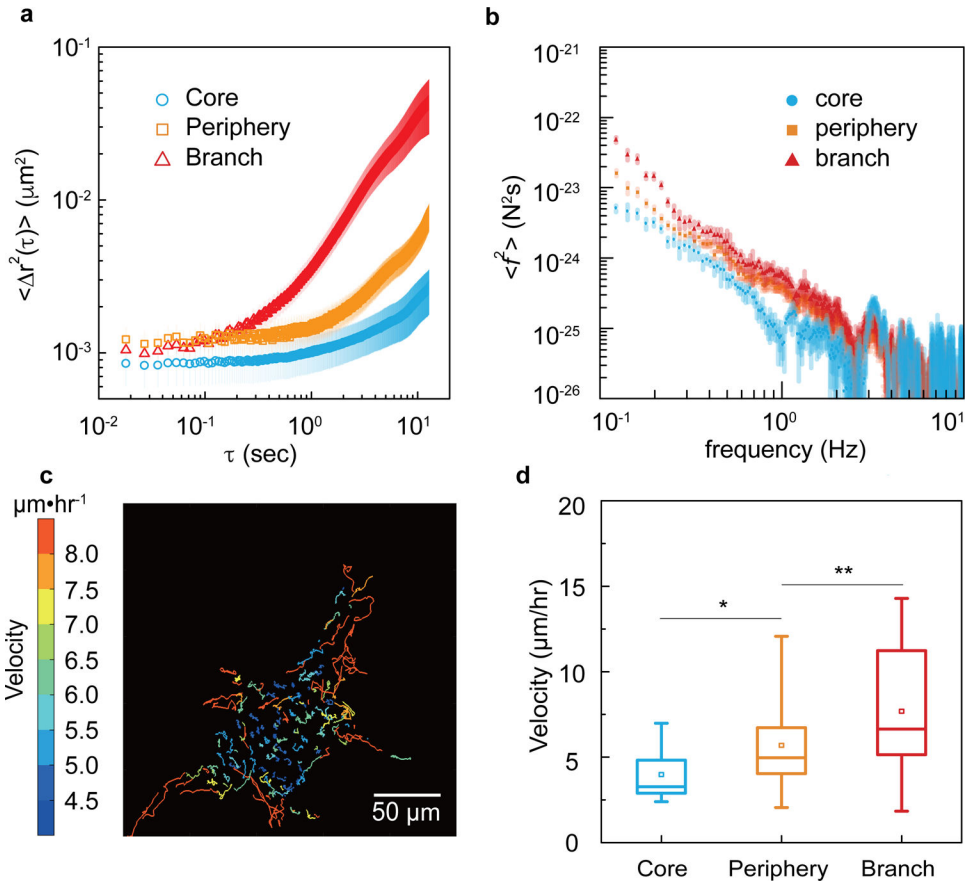

Figure 2. Different cell subpopulations in a cancer organoid show distinct dynamic behaviors.

a, Two dimensional time- and ensemble-averaged MSD, $<\Delta r^2(\tau)>$, of 0.5-μm-diameter particles are plotted against lag time on a log-log scale, in the cytoplasm of cells in core (blue circles), periphery (orange squares) and branch (red triangles) regions of the cancer organoid. The data is averaged from 15 independent measurements and the error bars stand for standard deviation. **b**, Cytoplasmic force spectrum calculated from spontaneous fluctuations of tracer particles and the active microrheology measurements, through $<F^2(\omega)>=|K(\omega)|^2<r^2(\omega)>$ inside cells at different locations of the cancer organoid. Data are shown as mean ± standard deviation. (n>10). **c**, Cell migratory trajectories over 4 hours reveal a highly dynamic scenario of cell migration within the central 20-μm cross-section of the cancer organoid. The color stands for the average migratory speed of each cell. **d**, The migratory speed of cells in each subpopulations are plotted. *P<0.05; **P < 0.01; ***P<0.001.

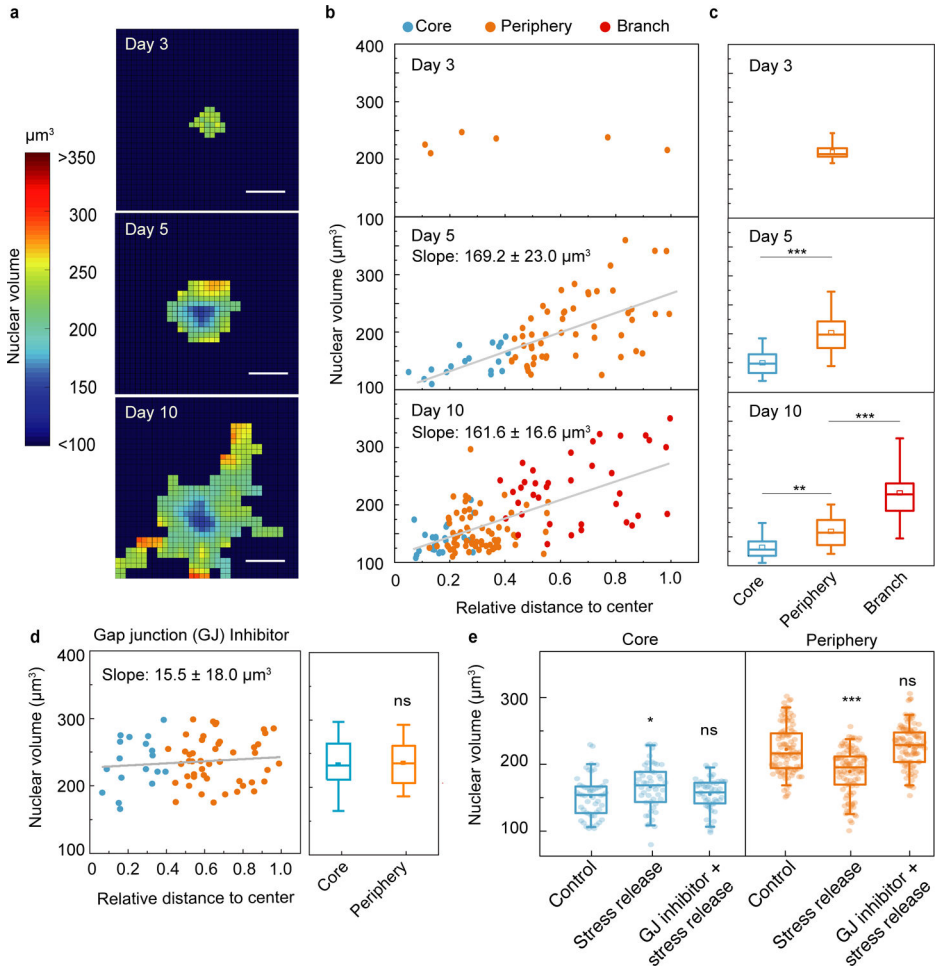

Figure 3. Temporal and spatial evolution of cell volume during the growth of cancer organoids.

a, Nuclear volume heat map shows the evolution of cell nuclear volume distribution in the developing cancer organoid. **b**, Nuclear volume of every individual cell in the cancer organoid is plotted against relative distance to the organoid center at different stages, showing a strong correlation between nuclear volume and spatial position, especially at middle and later stages. **c**, Nuclear volume of cells in different geometrical regimes of the cancer organoids (n>3). **d**, Nuclear volume of individual cells in GJ-inhibited cancer organoids. **e**, Stress release changes the distribution of individual nuclear volumes in the core and periphery if GJ are intact. Scale bars in **a** represent 50 μm. *P<0.05; **P < 0.01; ***P<0.001.

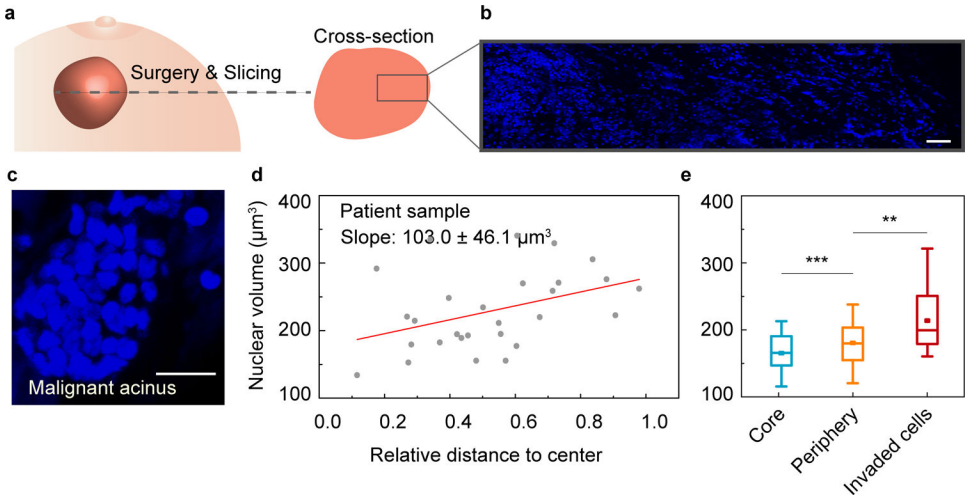

Figure 4. Characterization of cell volume heterogeneity in patient samples.

a, Schematic of a tumor biopsy from breast cancer patient. **b**, Large-scale fluorescent image showing cell nuclei from core to edge area of the biopsy. **c**, Invasive acinar structures within the biopsy. **d**, Individual cell nuclear volume is plotted against its relative distance to the center of the invasive acinar structure. **e**, Nuclear volume of cells in different geometrical regimes of the invasive acinar structures (n=3). Scale bars in **b** and **c** represent 50 and 20 μm, respectively. *P<0.05; **P < 0.01; ***P<0.001.

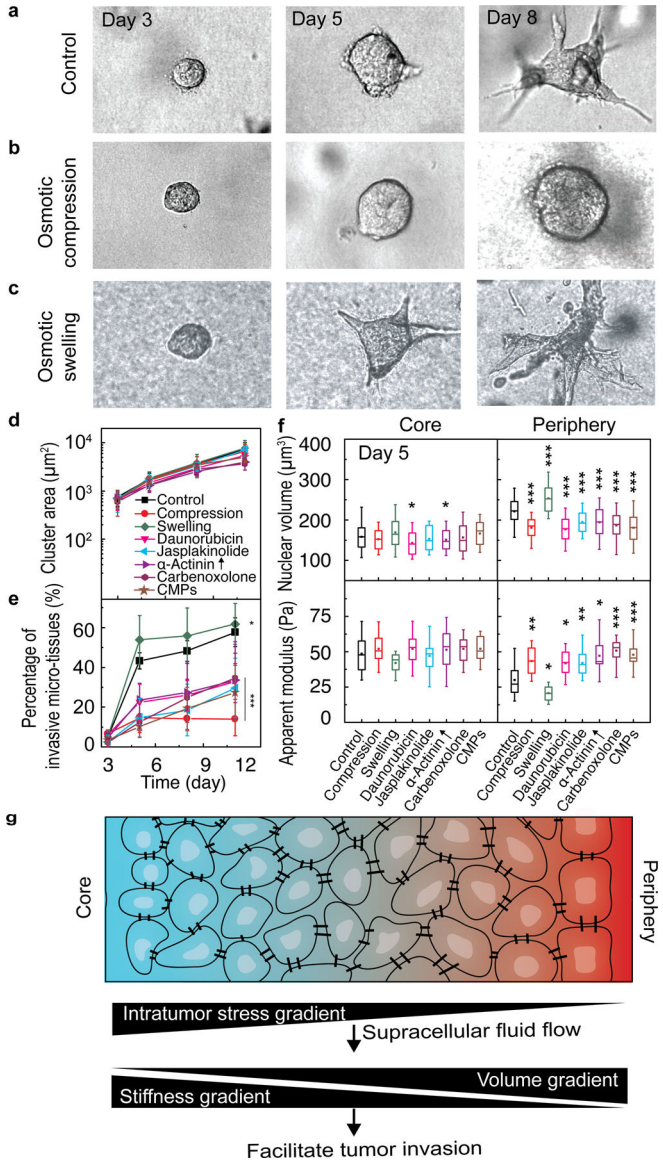

Figure 5. Stiffening the soft cell subpopulation inhibits the invasion of the tumor cells.

a-c, Bright-field images show the time-dependent morphological changes of the developing cancer organoids under different culture conditions, including complete culture medium (a), osmotic compression (b) and osmotic swelling (c). **d**, Quantification of the projected areas of cancer organoids shows the growth rate under different culture conditions are comparable. CMPs: connexin mimetic peptides. **e**, Percentage of the invasive cancer organoids over time under different culture conditions. Stars indicates the statistically significant difference between each groups and the control on day 11 **f**, Cell nuclear volume and cell stiffness in the core and periphery of the organoids under different conditions in d. **g**, Working hypothesis that the intratumor stress gradient drives supracellular fluid flow and thus results in cell volume and stiffness gradients, which together facilitate tumor cell invasion. *P<0.05;

P < 0.01; ***P<0.001. Scale bars in **a, **b** and **c** represent 50 μm. Error bars in **d** and **e** indicate standard deviation. Measurements are done in 3 independent experiments.